ISSN 2616-5880 Vol. 7, Issue 1: 89-101, DOI: 10.25236/AJMC.2026.070113

CFD–PBM Simulation of Multiphase Flow Component Combustion Synthesized Nanoparticles Using QMOM and TEMOM

Kai Wang[1,a,*]

[1]*College of Science, China Jiliang University, Hangzhou, 310018, China*
[a]*13957672537@163.com*
** Corresponding author*

Abstract: *Flame synthesis is a major method for controllable nanoparticle preparation, which involves coupled turbulence, heat-mass transfer and particle dynamic behaviors. Numerical simulation is an effective means to reveal its internal mechanism. This work establishes a coupled CFD-PBM framework to investigate TiO_2 nanoparticle formation via thermal decomposition of titanium tetraisopropoxide (TTIP) in a reacting flow reactor. The Reynolds-averaged Navier–Stokes (RANS) equations combined with standard k–ε model are adopted to solve gas flow, heat transfer and species transport in ANSYS Fluent. For particle population dynamics, two moment methods are applied: the built-in Quadrature Method of Moments (QMOM) is used for moment calculation and diagnostic analysis; the Taylor-expansion Method of Moments (TEMOM) is realized via four User-Defined Scalars (UDS) to achieve flexible moment closure. The model considers TTIP decomposition, TiO_2 nucleation, surface growth and Brownian coagulation. Simulation results identify key regions of particle formation and evolution, and compare the performance of QMOM and TEMOM. QMOM presents sharper moment peaks with high sensitivity to spatial variation, while TEMOM obtains smoother distribution, lower numerical dissipation and computational cost. The combined framework integrates the advantages of two methods, providing a reliable tool for mechanism analysis and parametric research of flame-synthesized nanoparticles.*

Keywords: *Turbulent reacting flow; QMOM; TEMOM; Population balance model; Nanoparticle coagulation*

1. Introduction

High-temperature flame reaction is widely used for nanomaterial synthesis in energy, environmental protection, catalysis and optoelectronics fields, featuring fast reaction speed, continuous production and good scalability[1]. Titanium dioxide (TiO_2) nanoparticles, as a typical functional material, are mainly produced by gas-phase combustion synthesis in coflow diffusion-flame reactors[2]. This type of reactor can form stable flame with controllable temperature and residence time, and is widely applied in the research of nanoparticle formation mechanism[3].Flame synthesis of nanoparticles is a complex multiscale process: strong temperature gradient leads to obvious spatial inhomogeneity of flow field; reactive flow is tightly coupled with particle nucleation, growth and coagulation. It is difficult to fully analyze the process only by experiments, so coupled CFD-PBM numerical simulation has become the mainstream research method.

In previous studies, scholars have continuously improved the CFD-PBM coupling system.Yu et al. (2007) conducted early numerical simulations of nanoparticle synthesis in diffusion-flame reactors, connecting reactive flow with particle evolution to predict particle inception and growth trends, and established a foundational paradigm for subsequent CFD–PBM coupled modeling[4]. For diffusion-flame reactor scenarios, He S et al. (2025) performed a combined experimental–numerical study on TiO_2 nanoparticle evolution, assessed the model's explanatory capability by comparing measurements and simulations[5]. Regarding PBM and moment methods, Bagheri et al. (2019) summarized typical PBM applications to nanoparticle formation, discussed equation formulations, key source terms, and numerical implementation issues, and highlighted the sensitivity of predictions to parameters and property assumptions[6]. At the TEMOM level, Chan et al. (2018) proposed and validated a bimodal TEMOM capable of describing nanoparticle formation and growth in turbulent flows, improving TEMOM's engineering applicability when multiscale size structures are present[7]. Mingliang X et al.(2022) developed TEMOM solutions and validations for the Smoluchowski equation governing Brownian

ISSN 2616-5880 Vol. 7, Issue 1: 89-101, DOI: 10.25236/AJMC.2026.070113

coagulation, providing methodological support for the accuracy and applicability limits of TEMOM in coagulation-dominated problems[8]. TEMOM applications have also expanded. Can T et al. (2021) applied TEMOM to simulate nucleation and aerosol evolution of vehicle emissions in background pollution fields, demonstrating TEMOM's efficiency in complex coupled environments[9]. Furthermore, Chen J et al. (2025) used TEMOM to characterize nanoparticle transport properties, indicating that TEMOM can be employed not only for macroscopic prediction of size distributions but also for statistical descriptions of particle dynamic behaviors in broader engineering problems[10]. In more general CFD–PBM coupling applications, Yang X et al. (2026) combined CFD–PBM analysis with interpretable machine learning to extract heat-transfer enhancement mechanisms from large operating-condition datasets, illustrating the potential of PBM at the interface of mechanistic modeling and data-driven validation[11]. Liang J et al. (2026) presented a three-dimensional CFD–PBM study in bubble columns, emphasizing the strong coupling between PBM and interphase momentum-exchange models. This suggests that in strongly coupled systems such as flame reactors, it is likewise essential to account for chain effects from changes in flow structure to changes in PBM source terms and ultimately to changes in particle properties[12]. As the core algorithm of PBM, moment methods have developed from basic calculation to low-cost, high-stability and interpretable simulation[13]. QMOM is a classic moment solution method built in mainstream CFD software. TEMOM, based on Taylor expansion, realizes analytical closure of population balance equation, and has been gradually applied to turbulent flow, vehicle exhaust aerosol and other complex coupled scenarios. Existing research shows that moment methods have unique advantages in CFD coupling, but there are still challenges including temperature-induced reaction uncertainty, coagulation kernel deviation and numerical stiffness of moment equations[14].

Current research has formed a mature technical route: using CFD to calculate flow, temperature and species field, and adopting PBM and moment methods to describe particle evolution[15]. For flame-synthesized metal oxide nanoparticles, accurate simulation must capture high-temperature reaction zone and downstream condensation region, and verify nucleation, growth and coagulation parameters[16]. On this basis, this paper constructs a CFD-PBM framework combining QMOM and TEMOM, simulates TiO_2 nanoparticle formation in a coflow reactor, compares the characteristics of two moment methods, and analyzes the influence of operating conditions on particle dynamic behaviors[17].

2. Mathematical Model

2.1. Gas-phase governing equations

The turbulent reacting flow in the reactor is described by RANS equations, including continuity equation, momentum equation, energy equation and species transport equation, which are the basic control equations for continuous gas phase.

1) Continuity equation

$$\frac{\partial \rho}{\partial \mathrm{t}} + \nabla \bullet (\rho u) = 0 \tag{1}$$

Here, ρ denotes the mixture density and u the mean velocity vector. For high-temperature reacting flows, ρ typically varies significantly with temperature and species composition. Therefore, the density is updated through an equation of state coupled with the local species and temperature fields, which more realistically captures the flow response induced by thermo-fluid–chemical interactions

2) Momentum equation

$$\frac{\partial (\rho u)}{\partial \mathrm{t}} + \nabla \bullet (\rho u u) = -\nabla p + \nabla \bullet \tau_{\mathrm{eff}} \tag{2}$$

Here, p is the pressure and τ_{eff} is the effective stress tensor. Under the eddy-viscosity assumption, the effective viscosity is expressed as $\mu_{eff}=\mu+\mu_t$, where μ is the laminar dynamic viscosity and μ_t is the turbulent viscosity. In this work, μ_t is obtained from the standard k–ε turbulence model, which is used to close the Reynolds stresses and to account for turbulence-enhanced momentum transport

3) Energy equation

$$\frac{\partial (\rho \mathrm{h})}{\partial \mathrm{t}} + \nabla \bullet (\rho \mathrm{h} u) = \nabla \bullet [(\lambda + \lambda_{\mathrm{t}}) \nabla \mathrm{T}] + \dot{\omega}_{\mathrm{h}} \tag{3}$$

ISSN 2616-5880 Vol. 7, Issue 1: 89-101, DOI: 10.25236/AJMC.2026.070113

Here, h is the specific enthalpy, T is the temperature, λ and λ_t denote the laminar and turbulent thermal conductivities, respectively, and ω_h represents the volumetric heat source induced by chemical reactions. In high-temperature, fast-reacting systems, there exists strong coupling between the reaction heat release and the temperature field: an increase in temperature alters reaction rates and transport properties, which in turn affects the local heat-release intensity and the flow structure. Therefore, the energy equation and species transport equations must be solved in a fully coupled manner with the reaction kinetics

4) Species transport equation

$$\frac{\partial(\rho Y_i)}{\partial t} + \nabla \bullet (\rho h Y_i) = -\nabla \bullet J_i + \dot{\omega}_i \tag{4}$$

Here, J_i is the diffusive flux of species i and ω_i is the net mass production rate of species i due to gas-phase chemical reactions. To account for the combined effects of molecular diffusion and turbulent mixing on scalar transport within the RANS framework, the diffusive flux is formulated in terms of an effective diffusion.

2.2. Chemical Reaction Model

This study adopts a global one-step reaction to describe TTIP thermal decomposition: TTIP decomposes at high temperature to generate solid TiO_2 nanoparticles and gaseous by-products. The total reaction rate includes homogeneous gas-phase reaction and heterogeneous surface reaction. The reaction rate constants are expressed by temperature-dependent empirical formulas, which conform to the exponential growth law of reaction rate with temperature in high-temperature system. This simplified reaction mechanism reduces calculation cost while retaining the main coupling relationship between precursor consumption and particle generation.

$$TTIP_{(gas)} \xrightarrow{k_g} TiO_2 + 4C_3H_6 + 2H_2O \tag{5}$$

$$TTIP_{(particle\,surface)} \xrightarrow{ks} TiO_2 + 4C_3H_6 + 2H_2O \tag{6}$$

The following is the overall global reaction for TTIP, and the corresponding reaction source term is given by:

$$\omega = kY_i = (k_g + k_s A)\ Y_i \tag{7}$$

Here, k is the overall decomposition rate constant of TTIP; k_g is the rate constant for the homogeneous gas-phase reaction; k_s is the rate constant for the heterogeneous surface reaction; A denotes the total particle surface-area concentration; and Y_i is the remaining TTIP concentration in the system.The rate constants k_g and k_s are typically described by temperature-dependent empirical correlations to reflect the exponential increase of decomposition/reaction rates with T at elevated temperatures.

$$k_g = 3.96e5 \times \exp(-8479.7 / T) \tag{8}$$

$$k_s = 1e9 \times \exp(-8479.7 / T) \tag{9}$$

Here, T denotes the gas temperature. This formulation is commonly used in engineering CFD reacting-flow simulations to close the overall reaction rate, and is suitable for high-temperature decomposition and oxidation systems with heat transfer.

2.3. Population Balance Model

2.3.1. QMOM Principle

Population balance equation (PBE) is used to describe the evolution of particle size distribution. The source terms in PBE are determined by three core processes: nucleation, surface growth and Brownian coagulation.

$$\frac{\partial f}{\partial t} + \nabla \bullet (uf) = B_{nuc}(v) - D_{nuc}(v) + B_{coag}(v) - D_{coag}(v) + B_{grow}(v) - D_{grow}(v) \tag{10}$$

Here, B and D denote the birth and death terms, respectively, arising from processes such as nucleation, coagulation, and surface growth. The k-th moment of the volume distribution is defined as:

ISSN 2616-5880 Vol. 7, Issue 1: 89-101, DOI: 10.25236/AJMC.2026.070113

$$M_k(t) = \int_0^\infty v^k f(v,t)dv, k = 0,1,2,..... \tag{11}$$

Here, m_0 is directly related to the particle number density. m_1 corresponds to the total particle volume concentration; if the solid-phase density is approximately constant, it is also proportional to the mass concentration. m_2 is associated with a measure of the total particle surface area. Combining with Eq. (10), multiplying both sides by v^k and integrating over the entire volume domain yields the moment transport equation and the expressions for the three source terms associated with nucleation, coagulation, and surface growth:

$$\begin{aligned}&\frac{\partial m_k}{\partial t} + \frac{\partial (u_j + (u_{th})_j)mk}{\partial x_j} \\ &= \frac{\partial}{\partial x_j}(\Gamma \frac{\partial m_k}{\partial x_j}) + k\int_0^\infty v^{k-1} G(v)N(v,t)dv + J(vp){v_p}^k \\ &+ \frac{1}{2}\int_0^\infty \int_0^\infty [(v+v')^k - v^k - v'^k]\beta(v,v')N(v,t)N(v',t)dvdv'\end{aligned} \tag{12}$$

In this work, J denotes the nucleation rate of primary particles, and G denotes the surface growth rate; the effect of coagulation is governed by the coagulation kernel. The specific forms and parameters of J, G, and the coagulation kernel are implemented via user-defined functions (UDF), enabling coupling with operating conditions and with the flow and thermal fields. J is linked to the formation rate of solid TiO2 and is specified in the model through a UDF. Its expression is given by:

$$J = k_g Y_i N_A \tag{13}$$

Here, Y_i is the molar concentration of TTIP, and N_A is Avogadro constant. the incorporation of the growth kernel within the PBM moment method is implemented via UDF.

$$G = k_s Y_i N_A V_{p0} A \tag{14}$$

Here, v_{p0} denotes the volume of a primary particle. For nanoscale particles, random collisions induced by Brownian motion constitute an important coagulation mechanism. In this work, a Brownian coagulation model is adopted, and the corresponding kernel function can be expressed as:

$$\beta(v_i, v_j) = \frac{2K_B T}{3\mu}\frac{(L_i + L_j)^2}{L_i L_j} \tag{15}$$

Here, K_B is the Boltzmann constant, T is the absolute temperature, μ is the fluid viscosity, and L_i is the particle diameter. The PBE is typically solved using the quadrature method of moments. QMOM approximates the distribution using a finite number of quadrature nodes v_n and weights w_n, such that the raw moments can be reconstructed in a discrete quadrature form as:

$$M_k = \sum_{n=1}^{NQ} w_n v_n^k \tag{16}$$

Here, N_Q denotes the number of quadrature nodes. Fluent solves the transport equations for w_n and v_n, and internally reconstructs the raw moments and their corresponding source-term fields.

2.3.2. TEMOM and UDS Implementation

Different from QMOM, the Taylor-expansion Method of Moments (TEMOM) expands particle size distribution function around characteristic volume to realize analytical closure of PBE integral terms. It only needs to solve low-order moments, with simpler equation form and stronger customizability. In this work, four UDS variables are defined in Fluent: m_0, m_1, m_2 and total particle surface area A. All UDS follow unified convection-diffusion-source transport equations. The source terms of nucleation, growth and coagulation are compiled by UDF based on TEMOM analytical formula. The whole model is independent of Fluent built-in PBM, which is convenient for algorithm verification and parameter adjustment.

$$\frac{\partial(\rho\phi_j)}{\partial t} = \nabla \bullet (\Gamma \phi_j \nabla \phi_j) + S_{\phi_j} \tag{17}$$

Here, $\Gamma_{\phi j}$ is the effective diffusion coefficient and $S_{\phi j}$ denotes the source term arising from nucleation, surface growth, and coagulation. The unknown particle size distribution function n(v) is expanded in a

ISSN 2616-5880 Vol. 7, Issue 1: 89-101, DOI: 10.25236/AJMC.2026.070113

Taylor series about a characteristic volume $\bar{v}$. The formulation can be written as:

$$n(v) \approx n(\bar{v}) + n'(\bar{v})(v-\bar{v}) + \frac{1}{2!}n''(\bar{v})(v-\bar{v})^2 + \frac{1}{3!}n'''(\bar{v})(v-\bar{v})^3 + \ldots\ldots \tag{18}$$

In the PBE framework, the coagulation source term corresponds to the Smoluchowski coagulation integral. TEMOM employs a Taylor expansion to express the coagulation source term in terms of low-order moments, thereby yielding an analytical closed-form expression that can be directly incorporated into the UDS equations:

$$\left\{\begin{array}{l}\frac{dM_0}{dt} = J + S^{(0)}_{coag}, \\ \frac{dM_1}{dt} = JV_{p0} + M_0 G, \\ \frac{dM_2}{dt} = S^{(2)}_{J+G} + S^{(2)}_{coag}\end{array}\right\} \tag{19}$$

$$\left\{\begin{array}{l} S^{(0)}_{coag} = B_2\left\{\frac{(2g^2-13g-151)}{81}M_0^{\,2} + \frac{\phi(5g^2-64g-103)}{81}M_0^{\frac{7}{3}}M_1^{-\frac{1}{3}}\right\}, \\ S^{(1)}_{coag} = 0, \\ S^{(2)}_{coag} = B_2\left\{-\frac{2(2g^2-13g-151)}{81}M_1^{\,2} + \frac{4\phi g\frac{1}{3}(g^2-2g-80)}{81}M_1^{\frac{7}{3}}M_2^{-\frac{1}{3}}\right\}\end{array}\right\}$$

2.4. Surface Area Model

Assuming primary particles are spherical, the equivalent diameter and initial surface area of newly nucleated particles are calculated by geometric formula. Considering particle sintering in high-temperature environment, the minimum surface area of aggregates and sintering characteristic time are introduced. The sintering time is related to activation energy, particle size and temperature. In this work, based on the prescribed initial particle volume and the assumption of sphericity, the equivalent diameter of a newly generated primary particle, d_{mono}, and its surface area, a_{p0}, are calculated, corresponding to Eqs. (20)–(21):

$$d_{mono} = \left(\frac{6V_{p0}}{\pi}\right)^{1/3} \tag{20}$$

$$a_{p0} = \pi d^2_{mono} \tag{21}$$

This minimum surface area is typically expressed in terms of the solved moments:

$$A_{min} = (\pi M_0)^{1/3}(6M_1)^{2/3} \tag{22}$$

Meanwhile, the mean particle size can also be represented in terms of moments, as given in Eq. (23):

$$d_p^* = \frac{6M_1}{A} \tag{23}$$

In the evolution of A, the surface-area decay rate of aggregates due to sintering is commonly governed by a characteristic time τ_f. Johannessen et al. [4] proposed the following approach: for two initially separate, contacting spherical primary particles, the characteristic coalescence time, defined as the time required for sintering to merge them into a common shape, is given by Eq. (24):

$$\tau_f = K_0(d_p^*)^m\left(\frac{T}{T_{ref}}\right)e^{\left[\frac{E_{AS}}{R}\left(\frac{1}{T}-\frac{1}{T_{ref}}\right)\right]} \tag{24}$$

Here, E_{AS} is the activation energy, d_p is the initial diameter of two contacting primary particles within an aggregate, k_0 is the pre-exponential factor referenced at the temperature T_{ref}, R is the universal gas constant, and m is the exponent. By combining Eqs. (20)–(24), a closed-form expression for the total surface area A per unit gas volume can be obtained:

ISSN 2616-5880 Vol. 7, Issue 1: 89-101, DOI: 10.25236/AJMC.2026.070113

$$\frac{dA}{dt} = Ja_{p0} - \frac{A - A_{min}}{\tau_f} \tag{25}$$

3. Numerical Simulation Method

3.1. Reactor Geometry and Operating Conditions

The simulation object is a two-dimensional axisymmetric coflow diffusion flame reactor with total axial length 0.11 m and diameter 0.14 m. The burner adopts three concentric tube inlets: the central tube transports carrier gas and TTIP precursor (inlet velocity 4.8 m/s); the middle annular channel inputs methane fuel (inlet velocity 1.63 m/s); the outermost channel supplies oxygen. To explore the influence of oxidizer flow rate, three working conditions are set: oxygen inlet velocities of 6.8 m/s, 13.6 m/s and 19.4 m/s (corresponding volume flow 2 L/min, 4 L/min, 6 L/min). The wall initial temperature is 450 K, and inlet turbulence intensity is 5%. The change of oxygen flow rate will adjust jet momentum, flame structure, reaction zone position and material residence time, and further affect particle formation.

3.2. Mesh and Mesh Independence Verification

Unstructured mesh is adopted for computational domain, and local encryption is carried out at inlet, shear layer, flame reaction zone and wall surface to capture sharp gradients of velocity, temperature and component concentration.

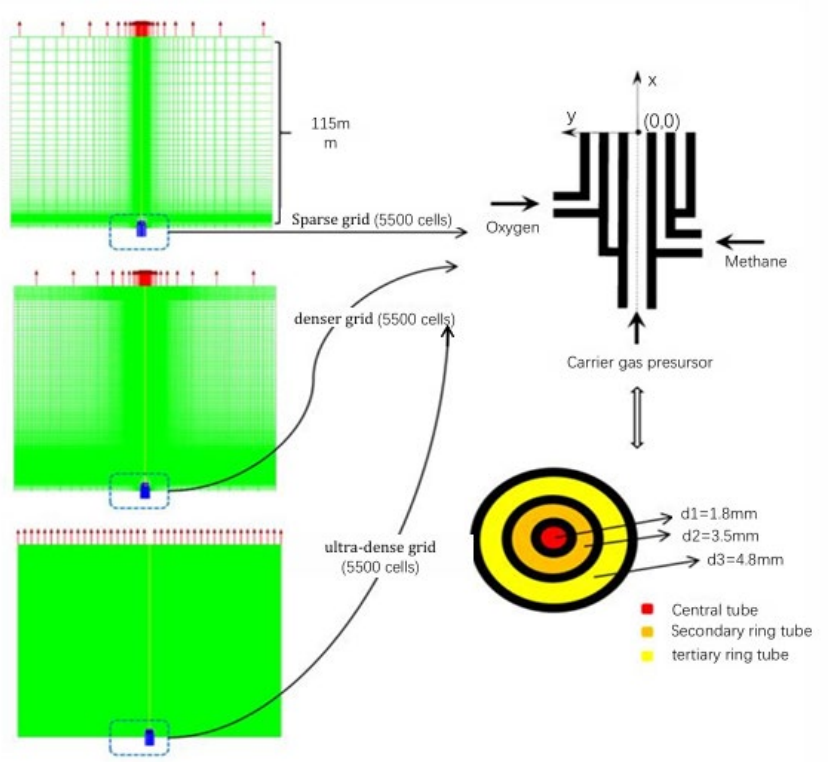

Figure 1: Burner configuration inlet plan view and simulation 2D modeling

As shown in Figure 1, three sets of meshes (5500 cells, 55000 cells, 550000 cells) are used for mesh independence test.

Table 1: Verification of key quantities across different meshes to ensure mesh independence

Grid number	5500	55000	550000
Temperature peak	2597K	2588K	2584K
particle number	3.79e+16	3.79e+16	3.79e+16

As shown in Table 1, the deviation of peak temperature and particle number concentration between medium mesh and fine mesh is less than 1%. Considering calculation accuracy and cost, the medium mesh (55000 cells) is selected for all simulation cases.

ISSN 2616-5880 Vol. 7, Issue 1: 89-101, DOI: 10.25236/AJMC.2026.070113

3.3. Solver Settings and Basic Assumptions

3.3.1. Turbulence and algorithm

Startand k–ε model with standard wall function is used for turbulence closure. Pressure-velocity coupling adopts Coupled algorithm. Convective terms use first-order upwind scheme, and diffusive terms use second-order central difference scheme. Gas phase is solved in steady state, and particle dynamics are transient calculation.

3.3.2. Model coupling

QMOM is enabled in Fluent PBM module, and TTIP consumption is calculated by built-in chemical reaction mechanism. Four UDS are added to realize TEMOM solution, and UDF is used to write particle dynamic source terms. QMOM and TEMOM run synchronously under the same flow and reaction field for comparative analysis.

3.3.3. Basic assumptions:

Tables must appear inside the designated margins.

1) Reactor internal flow is statistically steady turbulent flow; gas density changes with temperature and components.

2) Particle volume fraction is extremely low, only one-way coupling from gas phase to particles is considered.

3) Radiation heat transfer and complex surface reaction are ignored to simplify calculation.

4) Primary particle initial diameter is 0.4 nm, particles are spherical with constant density, and particle size is limited within nanoscale range.

4. Results and Discussion

4.1. Solver Settings and Basic Assumptions

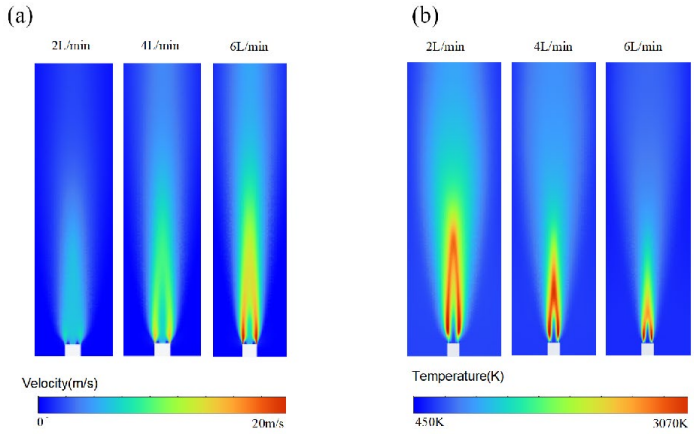

Figure 2: Flow rate and flame temperature distribution under different oxygen flow rates.(a)Contour plots of fluid velocity distribution under different oxygen flow rates.(b)Flame temperature distribution contour map under different oxygen flow rates.

ISSN 2616-5880 Vol. 7, Issue 1: 89-101, DOI: 10.25236/AJMC.2026.070113

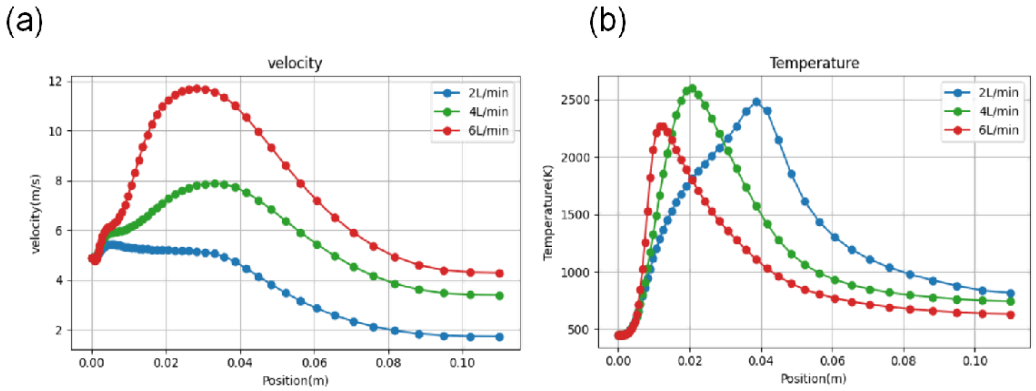

Figure 3: Flow velocity and flame temperature along the centerline under different oxygen flow rates.(a)Fluid velocity distribution along the centerline under different oxygen flow rates.(b)Temperature distribution of centerline flame under different oxygen flow rates.

Figure 2 shows velocity and temperature contours under different oxygen flow rates. All working conditions form typical coaxial jet structure. With the increase of oxygen flow rate, jet momentum enhances, the shear mixing between fuel and oxidizer intensifies, and velocity gradient in mixing layer becomes larger.

Figure 3 shows the change of oxygen flow rate significantly affects flame position and peak temperature: the higher the oxygen flow rate, the closer the high-temperature zone is to the inlet, and the peak temperature presents a decreasing trend. The difference of temperature field directly changes reaction rate and precursor conversion efficiency, which is the key factor affecting particle nucleation and growth.

4.2. TTIP Concentration Distribution

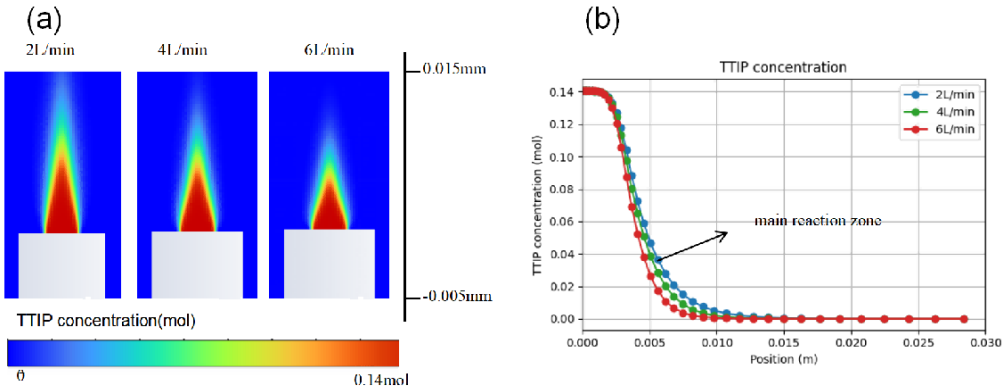

Figure 4: TTIP concentration distribution.(a)TTIP concentration distribution cloud map.(b)TTIP concentration centerline distribution

Figure 4 shows TTIP concentration reaches the maximum at the inlet, and decreases rapidly along the flow direction in the high-temperature reaction zone. The consumption area of TTIP is highly coincident with flame high-temperature area. Under high oxygen flow rate, TTIP is consumed more intensively near the inlet; under low flow rate, precursor gradually decomposes in a wider axial range. The distribution of precursor determines the spatial range of particle nucleation.

ISSN 2616-5880 Vol. 7, Issue 1: 89-101, DOI: 10.25236/AJMC.2026.070113

4.3. QMOM Calculation Results

4.3.1. Nucleation and Surface Growth Rate

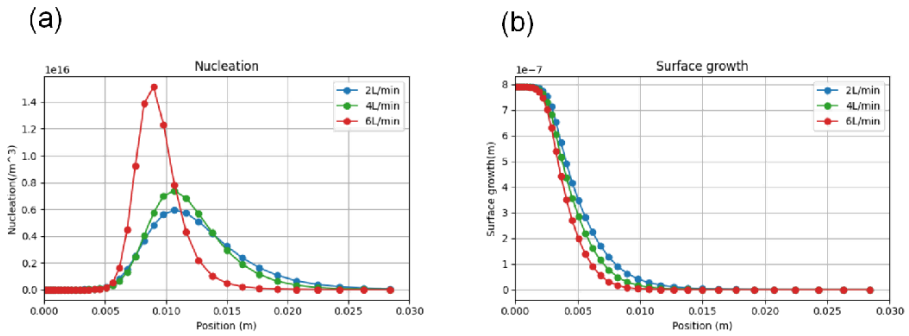

Figure 5: (a) Axial distribution of particle nucleation (b) Axial distribution of surface growth

Figure 5 shows particle nucleation rate and surface growth rate both reach the peak near the burner inlet, then decrease rapidly along the axial direction. With the increase of oxygen flow rate, the peak values of nucleation rate and growth rate increase obviously, and the attenuation speed accelerates. Under high flow rate, material residence time is shortened, and reaction and particle formation are concentrated in the upstream narrow area; under low flow rate, residence time is longer, and growth process extends to downstream area.

4.3.2. Distribution of Each Order Moment

Figure 6 shows m_0, m_1, m_2, m_3 calculated by QMOM all show obvious spatial non-uniformity: moments rise sharply in the high-temperature reaction zone, then decay downstream. Low-order moments are mainly affected by particle number (nucleation), while high-order moments are sensitive to large particles (growth and coagulation).

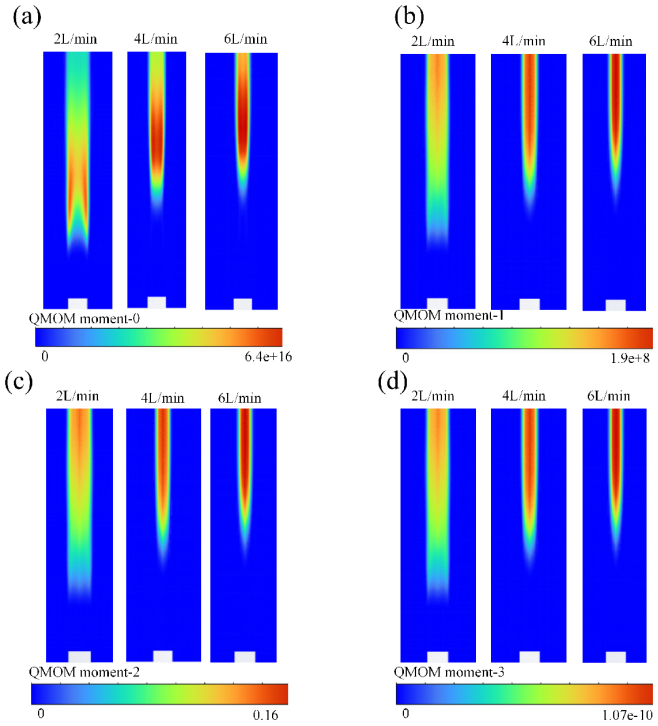

Figure 6: Spatial distribution of the fourth-order moments of QMOM under different oxygen flow rates.(a) m_0.(b) m_1 (c) m_2 (d) m_3

ISSN 2616-5880 Vol. 7, Issue 1: 89-101, DOI: 10.25236/AJMC.2026.070113

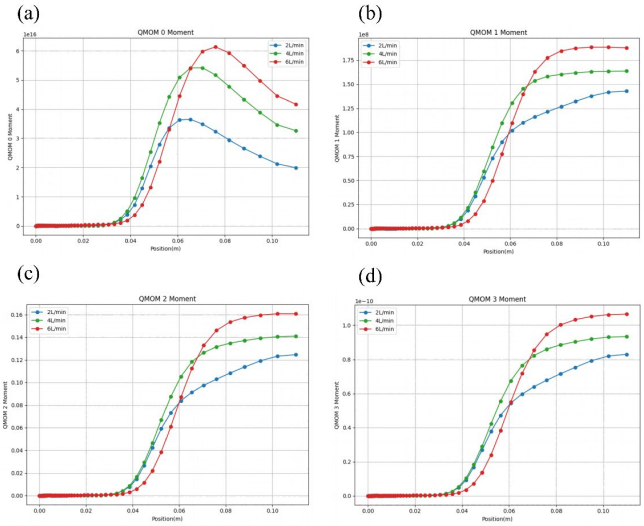

Figure 7: Spatial distribution of the third-order moments of QMOM under different oxygen flow rates.(a) m0.(b) m1 (c) m2 (d) m3

As shown in Figure 7, with the increase of oxygen flow rate, the peak of m_0 increases, the high-value area shrinks and moves upstream. Radial distribution shows that particle moments reach the maximum at the central axis, and decrease gradually to the surrounding area, which is consistent with the distribution law of temperature and precursor concentration.

4.4. TEMOM-UDS Calculation and Comparative Analysis

As shown in Figure 8 and Figure 9, the overall distribution rules of m_0, m_1, m_2 solved by TEMOM are consistent with QMOM, which verifies the reliability of two moment methods. The main differences are reflected in numerical characteristics:1) QMOM is more sensitive to local strong source terms, forming sharp peak distribution and obvious spatial contrast; 2) TEMOM based on Taylor expansion has smooth numerical characteristics, small local fluctuation and better stability. In engineering application, TEMOM has fewer solving variables, low computational cost, and is suitable for large-scale parametric research; QMOM can reconstruct detailed particle size distribution, which is applicable to the research requiring high precision of particle size information.

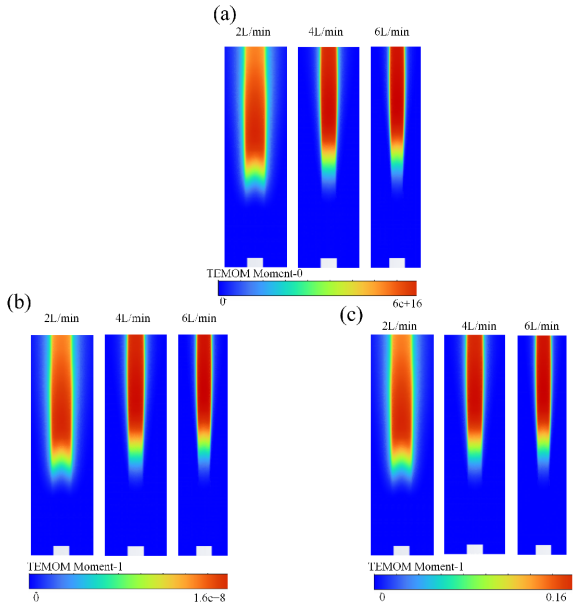

Figure 8: Spatial distribution of the third-order moments of TEMOM under different oxygen flow rates.(a) m0.(b) m1 (c) m2

ISSN 2616-5880 Vol. 7, Issue 1: 89-101, DOI: 10.25236/AJMC.2026.070113

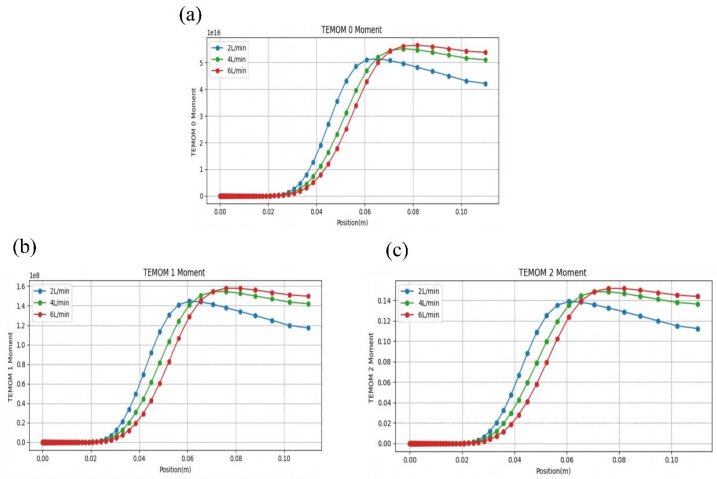

Figure 9: Spatial distribution of the third-order moments of TEMOM under different oxygen flow rates.(a) m0.(b) m1 (c) m2

4.5. Coagulation and Particle Characteristic Parameters

4.5.1. Coagulation Kernel and Total Surface Area

Figure 10 shows Brownian coagulation kernel B2 is positively correlated with temperature. The peak of coagulation kernel moves upstream with the increase of oxygen flow rate, and the coagulation intensity in downstream area decreases. It indicates that high oxygen flow rate makes coagulation occur earlier, but weakens the continuous coagulation effect in the rear of reactor. Total particle surface area first increases and then decreases along the axial direction. Low oxygen flow rate corresponds to higher surface area peak and backward peak position; high flow rate makes surface area peak decrease and move upstream. The change of surface area is the result of the competition between particle number increase and particle size enlargement.

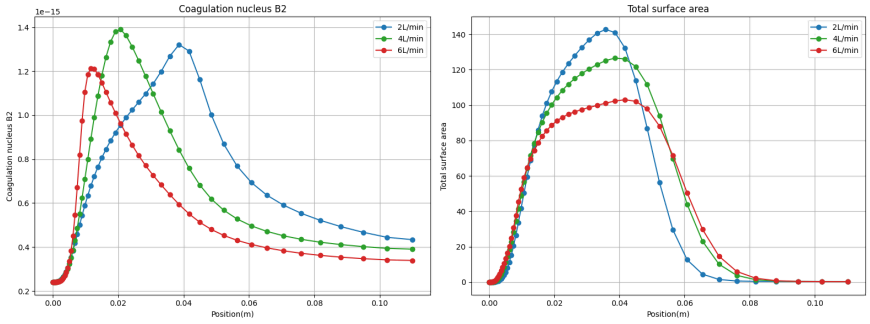

Figure 10: Axial distribution of coalescence kernel function B2 and total surface areaunder different oxygen flow rates

4.5.2. Particle Size Distribution

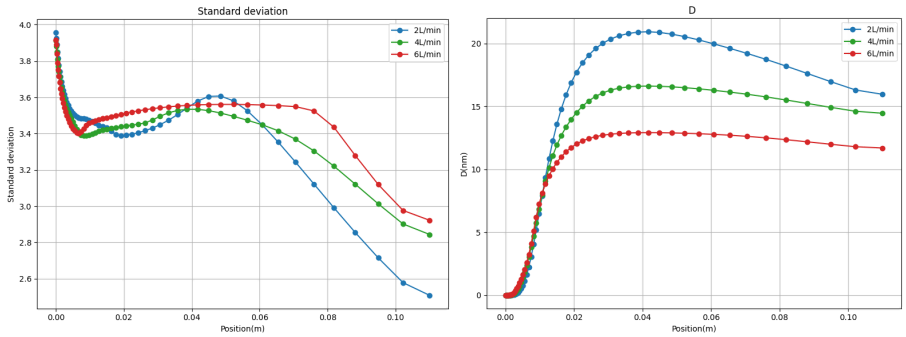

Figure 11: Axial distribution of geometric standard deviation σ_g and particle size distribution under different oxygen flow rates

ISSN 2616-5880 Vol. 7, Issue 1: 89-101, DOI: 10.25236/AJMC.2026.070113

Figure 11 shows Geometric standard deviation σ_g reflects particle size uniformity and Sauter mean diameter D_{32} reflects average particle size. Near the inlet, σ_g is large; downstream σ_g gradually decreases. Under high oxygen flow rate, the overall particle size dispersion is stronger. Particles grow rapidly in the upstream reaction zone and reach stable size; downstream growth slows down. Lower oxygen flow rate corresponds to larger average particle size, because longer residence time promotes particle coagulation and growth.

5. Conclusion

This paper constructs a CFD-PBM coupled framework combining QMOM and TEMOM, and numerically simulates TiO_2 nanoparticle synthesis by TTIP thermal decomposition in a coflow flame reactor. The main conclusions are as follows:

(1) The established model can synchronously predict gas-phase flow, temperature, precursor concentration and particle moment evolution. QMOM and TEMOM are mutually verified in calculation results, which can accurately capture the whole process from particle nucleation to growth and coagulation.

(2) Oxygen flow rate is a key operating parameter: increasing oxygen supply intensifies upstream reaction, improves particle nucleation intensity, makes reaction and particle formation concentrated near the inlet, and reduces the average particle size in the final product.

(3) Two moment methods have their own characteristics: QMOM has high spatial resolution and can reflect fine changes of particle distribution; TEMOM has good numerical stability, low calculation cost and flexible secondary development ability. The combination of the two methods can meet different simulation demands.

(4) The CFD-PBM framework proposed in this paper is suitable for the simulation of flame synthesis nanoparticles. On the basis of this research, detailed reaction mechanism, non-spherical particle model and large eddy simulation can be added in the follow-up work to further improve the simulation accuracy.

References

[1] Li S, Ren Y, Biswas P, et al. Flame aerosol synthesis of nanostructured materials and functional devices: Processing, modeling, and diagnostics[J]. Progress in Energy and Combustion Science, 2016, 5:51-59.

[2] Wang Y, Xie Y, Guo X, et al. Morphological convergence in solid-state synthesis: Unveiling the critical role of TiO2 precursor size for high-performance H2TiO3 lithium ion-sieves[J]. Particuology, 2026, 11:01-13.

[3] Ju J, Wu Y, Meng Y, et al. Multiscale numerical simulation of nano-TiO2 particle formation and evolution in an industrial flame reactor[J]. Chemical Engineering Science, 2026, 323:123244.

[4] Yu M, Lin J, Chan T. Numerical simulation of nanoparticle synthesis in diffusion flame reactor[J]. Powder Technology, 2007, 181(1): 9-20.

[5] He S, Shang C, Lu H, et al. Experimental and numerical study of TiO2 nanoparticle evolution in a diffusion flame reactor[J]. Combustion and Flame, 2025, 273: 113965.

[6] Bagheri H, Hashemipour H, Ghader S. Population balance modeling: application in nanoparticle formation through rapid expansion of supercritical solution[J]. Computational Particle Mechanics, 2019, 6(4): 721-737.

[7] Chan L T, Liu S, Yue Y. Nanoparticle formation and growth in turbulent flows using the bimodal TEMOM[J]. Powder Technology, 2018, 323: 507-517.

[8] Mingliang X, Qing H. Solution of Smoluchowski coagulation equation for Brownian motion with TEMOM[J]. Particuology, 2022, 70: 64-71.

[9] Can, T., et al., Simulation of Aerosol Evolution within Background Pollution for Nucleated Vehicle Exhaust via TEMOM[J]. Applied Sciences, 2021. 11(10): 4552–4552.

[10] Chen J, Li W, Li D, et al. Characterization of nanoparticle agglomerate motion based on the TEMOM method[J]. Powder Technology, 2025, 455: 120711.

[11] Yang X, Qian Z, Xie X, et al. Interpretable machine learning coupled with CFD-PBM analysis for heat transfer enhancement of ice slurry in SRTT[J]. International Communications in Heat and Mass Transfer, 2026, 172(4): 110461.

[12] Liang J, Xiong H, Hu Z, et al. Three-dimensional CFD-PBM insights into bubble dynamics and interfacial momentum transfer in bubble columns[J]. Separation and Purification Technology, 2026, 388:

ISSN 2616-5880 Vol. 7, Issue 1: 89-101, DOI: 10.25236/AJMC.2026.070113

136527.
[13] Fakharnezhad A, Kelesidis G, Berry J, et al. Nucleation, surface growth and coagulation of soot by hierarchical modeling[J]. Powder Technology, 2026, 469(1): 121747.
[14] Manis K L, Ge J, Kim A C, et al. Population Balance Models for Catalytic Depolymerization: From Elementary Steps to Multiphase Reactors. [J]. Accounts of chemical research, 2025, 58(12): 1847-1855.
[15] Bier R, Briesen H. Model reduction for 2D population balance models integrating particle shape dynamics: Theoretical derivation and application to crystallization systems[J]. Chemical Engineering Science, 2025, 318: 122087-122087.
[16] Sarigiannis D, Peck J, Mountziaris T, et al. Vapor Phase Synthesis of II-IV Semiconductor Nanoparticles in a Counterflow Jet Reactor[J]. MRS Proceedings, 2000, 616(1): 41.
[17] Shettigar A N, Bi Q, Toorman E. Assimilating Size Diversity: Population Balance Equations Applied to the Modeling of Microplastic Transport. [J]. Environmental science & technology, 2024, 58(36):16112-16120.